

# Demonstrating Ignition Hydrodynamic Equivalence in Direct-Drive Cryogenic Implosions on OMEGA

## Introduction

The main approach to ignition by means of inertial confinement fusion (ICF)<sup>1,2</sup> currently pursued at the National Ignition Facility (NIF)<sup>3</sup> is x-ray (or indirect) drive, where the laser energy absorbed in a high- $Z$  hohlraum is re-emitted in the form of x rays that drive the fuel capsule. In the other ICF approach—direct drive—the target is driven by laser irradiation directly coupled to the plasma blowing off the imploding capsule. The main advantage of the indirect-drive approach is reduced sensitivity of drive uniformity to short-scale beam nonuniformities. The main advantage of direct drive is a higher coupling efficiency (by factor of 3 to 5) of laser energy into kinetic energy of the shell (hydrodynamic efficiency) compared to that of x-ray drive. The OMEGA Laser System<sup>4</sup> and the KrF laser NIKE at the Naval Research Laboratory<sup>5</sup> have been the principal facilities for direct-drive experiments in the U.S.

Significant progress has been made over the last several decades in beam smoothing. This includes distributed phase plates (DPP's),<sup>6</sup> polarization smoothing with birefringent wedges,<sup>7</sup> smoothing by spectral dispersion (SSD),<sup>8</sup> and induced spatial incoherence.<sup>9</sup> In addition to these improvements, implementing adiabat shaping techniques<sup>10,11</sup> to significantly reduce Rayleigh–Taylor (RT) instability<sup>12,13</sup> growth during shell acceleration and demonstrating imprint mitigation with mid- $Z$ -doped ablaters<sup>14</sup> and high- $Z$  target overcoats<sup>15</sup> make the direct-drive approach very attractive. The progress in direct-drive research and the challenges in achieving ignition on the NIF using x-ray drive suggests that direct drive as a viable alternative for developing a burning-plasma platform in the laboratory be considered.

Compared to x-ray drive, direct-drive targets couple a larger fraction of laser energy into shell kinetic energy and internal energy of the neutron-producing central region of the target (hot spot) at peak fuel compression. Larger hot-spot energy relaxes the requirement on shell convergence and hot-spot pressure in an igniting target. This can be shown with the help of a commonly used ignition condition according to which plasma self-heating is initiated by both  $PdV$  work and alpha-particle

deposition inside the hot spot, given the product of areal density and ion temperature satisfies<sup>1,2,16,17</sup>

$$(\rho R)_{\text{hs}} \times T \gtrsim 0.3 \text{ g/cm}^2 \times 5 \text{ keV}, \quad (1)$$

where  $\rho$ ,  $R_{\text{hs}}$ , and  $T$  are the hot-spot density, radius, and temperature, respectively. Substituting expressions for the pressure  $\rho_{\text{hs}} = (1 + Z) \rho T / m_i$  ( $Z$  is the average ion charge and  $m_i$  is the average ion mass) and internal energy  $E_{\text{hs}} = 3/2 \rho_{\text{hs}} V_{\text{hs}}$  ( $V_{\text{hs}}$  is the neutron-averaged hot-spot volume) into Eq. (1) gives a minimum pressure requirement (threshold) for ignition,

$$p_{\text{hs}} > p_{\text{thr}} = 250 \text{ Gbar} \left( \frac{E_{\text{hs}}}{10 \text{ kJ}} \right)^{-1/2}, \quad \text{or}$$

$$\bar{P} = \frac{p_{\text{hs}}}{p_{\text{thr}}} = \left( \frac{p_{\text{hs}}}{250 \text{ Gbar}} \right) \sqrt{\frac{E_{\text{hs}}}{10 \text{ kJ}}} > 1, \quad (2)$$

where  $\bar{P}$  is the ignition pressure parameter.

Figure 145.30 shows the dependence of the threshold pressure  $p_{\text{thr}}$  on the hot-spot internal energy. Spherically symmetric direct-drive cryogenic designs on OMEGA couple up

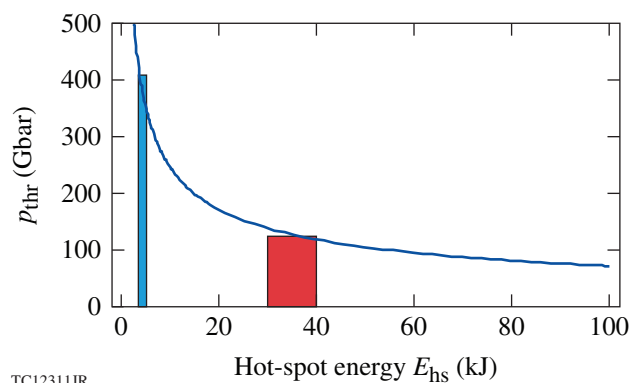


Figure 145.30

Threshold hot-spot pressure  $p_{\text{thr}}$  as a function of the hot-spot internal energy. A typical hot-spot energy in an indirect- and a direct-drive implosion for a National Ignition Facility (NIF)—scale laser energy is shown by the blue- and red-shaded regions, respectively.

to 0.44 kJ (out of 26-kJ incident laser energy) into the hot-spot internal energy. Hydrodynamically scaled to the NIF, with a laser energy of 1.5 MJ to 1.8 MJ, these designs are predicted to couple  $5\times$  to  $10\times$  more energy into the hot spot (25 kJ to 40 kJ, depending on laser coupling efficiency; see the red-shaded region in Fig. 145.30) compared to that of indirect drive (4 kJ to 5 kJ; see the blue-shaded region in Fig. 145.30), resulting in  $2.5\times$  to  $3\times$  lower hot-spot pressures required for ignition ( $\sim 120$  Gbar to 150 Gbar for direct drive versus 350 Gbar to 400 Gbar for indirect drive). The required hot-spot size also becomes smaller with a reduction in  $E_{\text{hs}}$ . According to Eq. (2) the hot-spot size scales as a square root of the internal energy, leading to a hot-spot size that is a factor of 2.5 to 3 larger in a direct-drive implosion compared to an x-ray-drive implosion.

### OMEGA Cryogenic Implosions

To separate 1-D factors limiting the target performance (drive efficiency, adiabat, etc.) from 3-D effects, a series of dedicated experiments was performed on OMEGA with the purpose of improving the accuracy of 1-D code predictions. To identify critical implosion parameters, the 1-D scaling laws for peak pressure, hot-spot energy, and the ignition-pressure parameter are written in terms of implosion velocity  $v_{\text{imp}}$  (defined as the peak mass-averaged shell velocity), the drive (ablation) pressure  $p_{\text{abl}}$ , and in-flight shell adiabat  $\alpha$  (Ref. 18),

$$\begin{aligned} p_{\text{hs}}^{1\text{-D}} &\sim \frac{p_{\text{abl}}^{1/3} v_{\text{imp}}^{10/3}}{\alpha}, \\ E_{\text{hs}}^{1\text{-D}} &\sim E_{\text{kin}} \frac{v_{\text{imp}}^{4/3}}{\alpha^{2/5} p_{\text{abl}}^{4/15}}, \\ \bar{P}^{1\text{-D}} &\sim \frac{\sqrt{E_{\text{kin}}} v_{\text{imp}}^4 p_{\text{abl}}^{1/5}}{\alpha^{6/5}}. \end{aligned} \quad (3)$$

The implosion velocity and shell kinetic energy  $E_{\text{kin}}$  are inferred in an experiment by measuring the ablation-front trajectory and mass ablation rate using self-emission imaging.<sup>19</sup> The ablation pressure is inferred from simulations that match the measured ablation-front trajectory, mass ablation rate, bang time,<sup>20</sup> and scattered-light power and spectrum.<sup>21</sup> Finally, the shock-induced adiabat is inferred by measuring shock velocities early in the pulse using VISAR (velocity interferometer system for any reflector).<sup>22</sup> An additional fuel-adiabat increase caused by hot-electron preheat is estimated by measuring the hard x-ray signal<sup>23</sup> and areal density<sup>24,25</sup> in mid- to high-adiabat implosions (the areal density in 1-D, for a given laser energy, depends mainly on the shell adiabat,<sup>26</sup>  $\rho R \sim \alpha^{-0.5}$ ). The estimate of the

shell-preheat effect based on the areal-density measurement is valid only for implosions with  $\alpha \gtrsim 3.5$  since shell integrity and fuel compression in lower-adiabat implosions are compromised because of the short-scale mix. A detailed comparison of 1-D simulation results using the hydrocode *LILAC*<sup>27</sup> with the data<sup>18</sup> shows good agreement between the two for a variety of target designs and drive conditions. One-dimensional simulations include the nonlocal thermal-transport model,<sup>28</sup> the ray-based cross-beam energy transfer (CBET) model,<sup>29</sup> and first-principle equation-of-state models<sup>30</sup> for both DT ice and the CD ablator.

An analysis of direct-drive implosions on OMEGA has shown that coupling losses caused by CBET<sup>29</sup> significantly reduce the ablation pressure (as much as 40% on OMEGA and up to 60% on the NIF-scale targets), implosion velocity, and shell kinetic energy. Including such losses, a demonstration of the hydrodynamic equivalence of implosions on OMEGA to ignition designs on the NIF requires that the shell's in-flight aspect ratio exceed the current stability threshold level ( $\sim 22$ ) (Ref. 18). One of the CBET mitigation strategies<sup>31</sup> involves using laser illumination with a laser-beam diameter smaller than the initial shell diameter. This, as demonstrated both theoretically and experimentally, recovers some coupling losses and increases the ablation pressure. Since the effect of CBET is small early in the implosion, when the density scale length and laser intensity are small, beam-zooming schemes<sup>32</sup> can be considered when the beam's focal spot at an early time is at the initial target radius (to maximize the illumination uniformity), then reduced down to  $0.6\times$  to  $0.7\times$  of the size at the beginning of the main drive.

While the implementation of zooming on OMEGA is still a few years away, a test of the CBET reduction strategy was performed using "static" DPP's, which produces focal spots smaller than the initial target size throughout the entire drive pulse. New distributed phase plates (called SG5, after the super-Gaussian order of the focal-spot profile being close to 5) were designed and installed on OMEGA with the purpose of studying CBET mitigation techniques. These plates have a lower focal-spot nonuniformity level compared to the existing DPP's (so-called SG4). The focal-spot radius was fixed at  $R_b = 410 \mu\text{m}$  (95% of laser energy is encircled within radius  $R_b$ ). The ratio of  $R_b$  to target radius ( $R_t$ ) was changed by varying  $R_t$  from  $400 \mu\text{m}$  to  $500 \mu\text{m}$ . Also, on-target UV energy (available to implode larger targets) was increased by implementing multiple-pulse driver lines (MPD) on OMEGA. In the MPD mode, SSD is turned off during the main pulse, making it possible to increase the UV energy from 26 kJ up to 29 kJ. In this configuration, however, the focal spot becomes slightly elliptical (or more accurately, the 2-D super-Gaussian fit of the focal-spot profile has an azimuthal variation in

the super-Gaussian order). The azimuthally averaged focal-spot profile has  $n_{SG} = 6.14$  and  $R_b = 388 \mu\text{m}$ . Using the MPD configuration for larger targets with  $R_t = 450 \mu\text{m}$ ,  $480 \mu\text{m}$ , and  $500 \mu\text{m}$  and the SSD driver for targets with  $R_t = 400 \mu\text{m}$ ,  $430 \mu\text{m}$ , and  $450 \mu\text{m}$ , the ratio  $R_b/R_t$  changed from 1.025 to 0.78. According to simulation results (that matched the observables), the smallest target ( $R_t = 400 \mu\text{m}$ ) has a  $v_{imp} = 3.5$  to  $3.6 \times 10^7$  cm/s and hydrodynamic efficiency (the ratio of the shell's kinetic energy to the total laser energy) of  $f_{hydro} = 3.5\%$ , while the largest target has a similar implosion velocity,  $v_{imp} = 3.6$  to  $3.7 \times 10^7$  cm/s, but more than twice the hydroefficiency,  $f_{hydro} = 7.2\%$ . Such an increase in hydroefficiency is caused partially by smaller refraction losses experienced by a larger target (smaller  $R_b/R_t$  and larger density scale length) and partially by reduced CBET losses. To quantify each effect, a simulation was performed with  $R_t = 500 \mu\text{m}$ , where  $R_b$  was increased to match  $R_t$ . In such a simulation, the implosion velocity was dropped by 17% to  $v_{imp} = 3 \times 10^7$  cm/s and the shell's hydrodynamic efficiency was reduced by 20% down to  $f_{hydro} = 5.8\%$ .

Figure 145.31 shows target performance for different target diameters. The hot-spot pressure is inferred<sup>33</sup> by using the measured neutron yield, burn duration  $\Delta t_{burn}$  (using both neutron time-of-flight and framing-camera measurements of x-ray burn duration), neutron-averaged ion temperature  $(T_i)_n$ , and hot-spot size  $R_{17}$  (defined as the radius of 17% of the peak-emission contour for x rays in the 4-keV to 7-keV energy range) at bang time using a time-resolved Kirkpatrick–Baez framing camera.<sup>34</sup> Assuming an isobaric hot spot and fitting the burn history to a Gaussian with full width at half maximum (FWHM) =  $\Delta t_{burn}$ , the maximum burn rate  $N_{max}$  relates to neutron yield  $Y$  as  $N_{max} = 2Y\sqrt{\ln 2/\pi}/\Delta t_{burn}$ , where  $N_{max} = n_T n_D T^2 \int_{V_{hs}} dV \langle \sigma v \rangle / T^2$ . Therefore, pressure at bang time can be determined using

$$p_{hs} \simeq \left[ 8Y\sqrt{\ln 2/\pi} / \left( f_D f_T \Delta t_{burn} \int_{V_{hs}} dV \langle \sigma v \rangle / T^2 \right) \right]^{1/2}, \quad (4)$$

where  $\langle \sigma v \rangle$  is the cross section for D–T reactions, and  $f_D$  and  $f_T$  are the fractions of D and T in the fuel, respectively. In evaluating the spatial integral in Eq. (4) the following spatial profile for the ion temperature (obtained using simulation results) is assumed:

$$T(r) = T_c \left[ 1 - (r/R_{hs})^2 (1 - 0.15^{3/2}) \right]^{2/3},$$

where  $T_c$  is the maximum hot-spot temperature, determined by matching

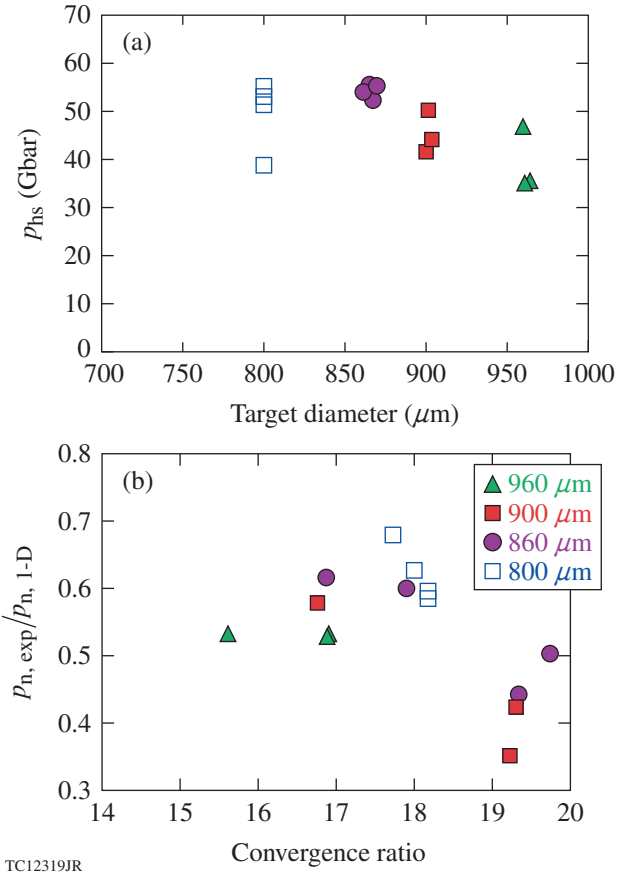


Figure 145.31

(a) Hot-spot pressure, inferred from experimental observables, as a function of target size. (b) Inferred hot-spot pressure normalized to 1-D code predictions versus the predicted shell convergence at 1-D bang time.

$$\left( \int_{V_{hs}} dV \langle \sigma v \rangle / T \right) / \left( \int_{V_{hs}} dV \langle \sigma v \rangle / T^2 \right)$$

with the measured  $(T_i)_n$ , and, as follows from code predictions,  $R_{hs}$  and measured  $R_{17}$  are related using  $R_{hs} = 1.06 R_{17}$ .

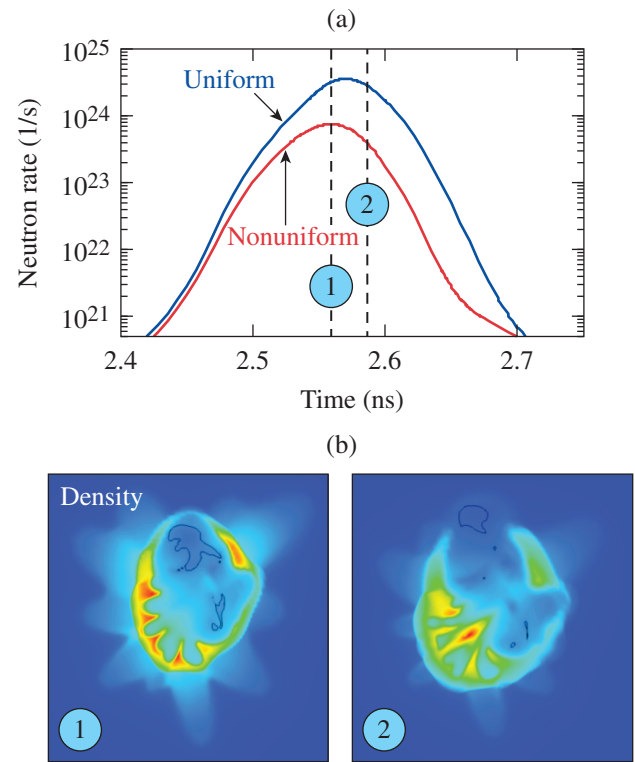
The following two conclusions can be made based on results shown in Fig. 145.31: first, the hot-spot pressure (both absolute and relative to 1-D predictions) degrades with the target size; second, there is a threshold of the shell's convergence ratio,  $CR^{1-D} \simeq 18$ , beyond which the hot-spot pressure normalized to the 1-D prediction drops from between 0.5 to 0.7 to between 0.3 to 0.5.

To understand these trends, one must consider the effects of shell nonuniformity. The evolution of long-wavelength nonuniformities seeded by target offset, beam geometry, beam power

imbalance, and mispointing is studied using the 3-D hydrocode *ASTER*.<sup>35</sup> This code includes 3-D hydrodynamics, ion and electron thermal conduction (the flux-limited Spitzer model), the CBET model, bremsstrahlung radiation losses, and nuclear reactivities. A simplified 3-D model of laser deposition is used, assuming a spherical symmetry of the plasma corona in the laser-deposition region, when performing ray tracing of individual beams (this approximation is justified because of strong lateral thermal-conduction smoothing in the high-temperature corona in direct-drive implosions). The beam power, timing, and pointing, however, can vary from beam to beam.

Simulations of cryogenic implosions on OMEGA show that the bubbles (areas of low-density material from the central region that protrude into the higher-density shell) developed because of the RT growth of long-wavelength perturbations ( $\ell \lesssim 5$ ) during shell deceleration, increasing the volume of the central region  $V_{\text{cntr}}$  and reducing the hot-spot pressure ( $p_{\text{hs}} \sim 1/V_{\text{cntr}}^{5/3}$ ) and neutron yield. As the shell converges further, the bubbles eventually break out of the shell, quenching hot-spot confinement and neutron yield. This is shown in Fig. 145.32. Since the burn truncates earlier because of the 3-D effects, the inferred hot-spot pressure reduces as a result of two effects: sampling and an increased volume  $V_{\text{cntr}}$  of the central region surrounded by the cold shell. Shifting the peak burn to an earlier time because of the nonuniformity growth samples earlier stages of hot-spot formation when shell convergence and the central pressure have not yet reached the peak values. The 3-D effects also increase the central region volume, preventing the fuel material from stagnating and effectively converting the shell kinetic energy into the internal energy of the hot spot. To account for the first effect (early pressure sampling), Fig. 145.33 plots the inferred hot-spot pressure normalized to the predicted pressure at the observed (earlier) bang time as a function of 1-D shell convergence calculated at the experimental bang time. Figure 145.33 shows that implosions with a fuel adiabat  $\alpha > 3.5$  proceed close to 1-D predictions up to a shell convergence of  $\text{CR} \sim 17$ . Further shell convergence does not lead to additional  $PdV$  work on the hot spot because of the RT growth of low- $\ell$  modes. An additional limitation on target performance at a lower fuel adiabat is caused by compromised shell integrity resulting from short-wavelength nonuniformity growth during shell acceleration.

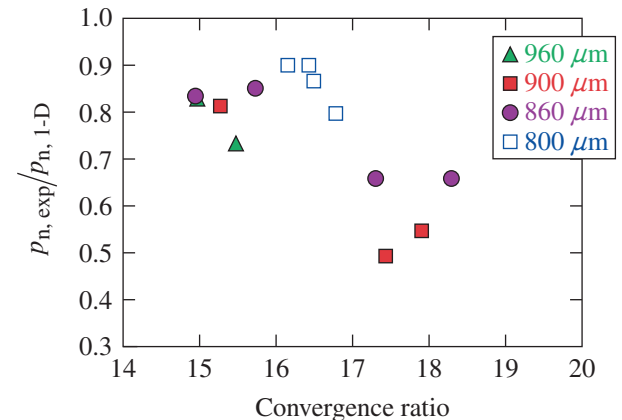
In summary, the cryogenic campaign with a reduced beam radius relative to the target radius ( $R_b/R_t < 1$ ), performed on OMEGA to reduce CBET losses, demonstrated increased laser coupling and hydrodynamic efficiency. This coupling enhancement, however, did not improve the target performance. Numerical simulations indicate that long-wavelength nonuni-



TC12376JR

Figure 145.32

(a) Neutron-production rate calculated using the code *ASTER* without (blue solid line) and with (red solid line) the effects of long-wavelength nonuniformity growth. (b) Simulated shell density maps at times indicated by (1) and (2).



TC12325JR

Figure 145.33

Inferred hot-spot pressure normalized to the 1-D predictions calculated at the experimental bang time versus 1-D shell convergence at the experimental bang time.

formities caused by target offset and power imbalance lead to an increased target central volume and early burn truncation. This effect is exacerbated by reduction in beam overlap when target size increases relative to beam size. Demonstrating hydrodynamic equivalence on OMEGA will require minimizing large-wavelength uniformities seeded by power imbalance and target offset and reusing target debris accumulated during cryogenic target production.

#### ACKNOWLEDGMENT

This material is based upon work supported by the Department of Energy National Nuclear Security Administration under Award Number DE-NA0001944, the University of Rochester, and the New York State Energy Research and Development Authority. The support of DOE does not constitute an endorsement by DOE of the views expressed in this article.

#### REFERENCES

- J. D. Lindl, *Inertial Confinement Fusion: The Quest for Ignition and Energy Gain Using Indirect Drive* (Springer-Verlag, New York, 1998).
- S. Atzeni and J. Meyer-ter-Vehn, *The Physics of Inertial Fusion: Beam Plasma Interaction, Hydrodynamics, Hot Dense Matter*, International Series of Monographs on Physics (Clarendon Press, Oxford, 2004).
- J. Paisner *et al.*, *Laser Focus World* **30**, 75 (1994).
- T. R. Boehly, D. L. Brown, R. S. Craxton, R. L. Keck, J. P. Knauer, J. H. Kelly, T. J. Kessler, S. A. Kumpan, S. J. Loucks, S. A. Letzring, F. J. Marshall, R. L. McCrory, S. F. B. Morse, W. Seka, J. M. Soures, and C. P. Verdon, *Opt. Commun.* **133**, 495 (1997).
- S. P. Obenschain *et al.*, *Phys. Plasmas* **3**, 2098 (1996).
- T. J. Kessler, Y. Lin, J. J. Armstrong, and B. Velazquez, *Proc. SPIE* **1870**, 95 (1993).
- T. R. Boehly, V. A. Smalyuk, D. D. Meyerhofer, J. P. Knauer, D. K. Bradley, R. S. Craxton, M. J. Guardalben, S. Skupsky, and T. J. Kessler, *J. Appl. Phys.* **85**, 3444 (1999).
- S. Skupsky, R. W. Short, T. Kessler, R. S. Craxton, S. Letzring, and J. M. Soures, *J. Appl. Phys.* **66**, 3456 (1989).
- R. H. Lehmburg and J. Goldhar, *Fusion Technol.* **11**, 532 (1987).
- V. N. Goncharov, J. P. Knauer, P. W. McKenty, P. B. Radha, T. C. Sangster, S. Skupsky, R. Betti, R. L. McCrory, and D. D. Meyerhofer, *Phys. Plasmas* **10**, 1906 (2003).
- V. N. Goncharov, T. C. Sangster, T. R. Boehly, S. X. Hu, I. V. Igumenshchev, F. J. Marshall, R. L. McCrory, D. D. Meyerhofer, P. B. Radha, W. Seka, S. Skupsky, C. Stoeckl, D. T. Casey, J. A. Frenje, and R. D. Petrasso, *Phys. Rev. Lett.* **104**, 165001 (2010).
- S. Chandrasekhar, in *Hydrodynamic and Hydromagnetic Stability*, International Series of Monographs on Physics (Clarendon Press, Oxford, 1961), p. 428.
- J. Sanz, *Phys. Rev. Lett.* **73**, 2700 (1994); V. N. Goncharov, R. Betti, R. L. McCrory, P. Sorotokin, and C. P. Verdon, *Phys. Plasmas* **3**, 1402 (1996).
- S. X. Hu, G. Fiksel, V. N. Goncharov, S. Skupsky, D. D. Meyerhofer, and V. A. Smalyuk, *Phys. Rev. Lett.* **108**, 195003 (2012).
- S. P. Obenschain *et al.*, *Phys. Plasmas* **9**, 2234 (2002).
- R. Betti, P. Y. Chang, B. K. Spears, K. S. Anderson, J. Edwards, M. Fatenejad, J. D. Lindl, R. L. McCrory, R. Nora, and D. Shvarts, *Phys. Plasmas* **17**, 058102 (2010).
- R. Betti, K. Anderson, V. N. Goncharov, R. L. McCrory, D. D. Meyerhofer, S. Skupsky, and R. P. J. Town, *Phys. Plasmas* **9**, 2277 (2002).
- V. N. Goncharov, T. C. Sangster, R. Betti, T. R. Boehly, M. J. Bonino, T. J. B. Collins, R. S. Craxton, J. A. Delettrez, D. H. Edgell, R. Epstein, R. K. Follet, C. J. Forrest, D. H. Froula, V. Yu. Glebov, D. R. Harding, R. J. Henchen, S. X. Hu, I. V. Igumenshchev, R. Janezic, J. H. Kelly, T. J. Kessler, T. Z. Kosc, S. J. Loucks, J. A. Marozas, F. J. Marshall, A. V. Maximov, R. L. McCrory, P. W. McKenty, D. D. Meyerhofer, D. T. Michel, J. F. Myatt, R. Nora, P. B. Radha, S. P. Regan, W. Seka, W. T. Shmayda, R. W. Short, A. Shvydky, S. Skupsky, C. Stoeckl, B. Yaakobi, J. A. Frenje, M. Gatu-Johnson, R. D. Petrasso, and D. T. Casey, *Phys. Plasmas* **21**, 056315 (2014).
- D. T. Michel, C. Sorce, R. Epstein, N. Whiting, I. V. Igumenshchev, R. Jungquist, and D. H. Froula, *Rev. Sci. Instrum.* **83**, 10E530 (2012).
- C. Stoeckl, V. Yu. Glebov, S. Roberts, T. C. Sangster, R. A. Lerche, R. L. Griffith, and C. Sorce, *Rev. Sci. Instrum.* **74**, 1713 (2003).
- W. Seka, D. H. Edgell, J. P. Knauer, J. F. Myatt, A. V. Maximov, R. W. Short, T. C. Sangster, C. Stoeckl, R. E. Bahr, R. S. Craxton, J. A. Delettrez, V. N. Goncharov, I. V. Igumenshchev, and D. Shvarts, *Phys. Plasmas* **15**, 056312 (2008).
- L. M. Barker and R. E. Hollenbach, *J. Appl. Phys.* **43**, 4669 (1972).
- C. Stoeckl, V. Yu. Glebov, D. D. Meyerhofer, W. Seka, B. Yaakobi, R. P. J. Town, and J. D. Zuegel, *Rev. Sci. Instrum.* **72**, 1197 (2001).
- J. A. Frenje, C. K. Li, F. H. Séguin, D. T. Casey, R. D. Petrasso, T. C. Sangster, R. Betti, V. Yu. Glebov, and D. D. Meyerhofer, *Phys. Plasmas* **16**, 042704 (2009).
- C. J. Forrest, P. B. Radha, V. Yu. Glebov, V. N. Goncharov, J. P. Knauer, A. Pruyne, M. Romanofsky, T. C. Sangster, M. J. Shoup III, C. Stoeckl, D. T. Casey, M. Gatu-Johnson, and S. Gardner, *Rev. Sci. Instrum.* **83**, 10D919 (2012).
- R. Betti and C. Zhou, *Phys. Plasmas* **12**, 110702 (2005).
- J. Delettrez, R. Epstein, M. C. Richardson, P. A. Jaanimagi, and B. L. Henke, *Phys. Rev. A* **36**, 3926 (1987).
- V. N. Goncharov, T. C. Sangster, P. B. Radha, R. Betti, T. R. Boehly, T. J. B. Collins, R. S. Craxton, J. A. Delettrez, R. Epstein, V. Yu. Glebov, S. X. Hu, I. V. Igumenshchev, J. P. Knauer, S. J. Loucks, J. A. Marozas, F. J. Marshall, R. L. McCrory, P. W. McKenty, D. D.

- Meyerhofer, S. P. Regan, W. Seka, S. Skupsky, V. A. Smalyuk, J. M. Soures, C. Stoeckl, D. Shvarts, J. A. Frenje, R. D. Petrasso, C. K. Li, F. Séguin, W. Manheimer, and D. G. Colombant, *Phys. Plasmas* **15**, 056310 (2008).
29. I. V. Igumenshchev, D. H. Edgell, V. N. Goncharov, J. A. Delettrez, A. V. Maximov, J. F. Myatt, W. Seka, A. Shvydky, S. Skupsky, and C. Stoeckl, *Phys. Plasmas* **17**, 122708 (2010).
  30. S. X. Hu, B. Miltzer, V. N. Goncharov, and S. Skupsky, *Phys. Rev. Lett.* **104**, 235003 (2010); S. X. Hu, L. A. Collins, V. N. Goncharov, J. D. Kress, R. L. McCrory, and S. Skupsky, *Phys. Rev. E* **92**, 043104 (2015).
  31. I. V. Igumenshchev, D. H. Froula, D. H. Edgell, V. N. Goncharov, T. J. Kessler, F. J. Marshall, R. L. McCrory, P. W. McKenty, D. D. Meyerhofer, D. T. Michel, T. C. Sangster, W. Seka, and S. Skupsky, *Phys. Rev. Lett.* **110**, 145001 (2013).
  32. D. H. Froula, T. J. Kessler, I. V. Igumenshchev, R. Betti, V. N. Goncharov, H. Huang, S. X. Hu, E. Hill, J. H. Kelly, D. D. Meyerhofer, A. Shvydky, and J. D. Zuegel, *Phys. Plasmas* **20**, 082704 (2013).
  33. C. Cerjan, P. T. Springer, and S. M. Sepke, *Phys. Plasmas* **20**, 056319 (2013).
  34. F. J. Marshall, V. N. Goncharov, V. Yu. Glebov, S. P. Regan, T. C. Sangster, and C. Stoeckl, the Ninth International Conference on Inertial Fusion Sciences and Applications (IFSA 2015), Seattle, WA, 20–25 September 2015 (Paper Th.Po.17).
  35. I. V. Igumenshchev, V. N. Goncharov, F. J. Marshall, J. P. Knauer, D. H. Froula, and S. P. Regan, “Three-Dimensional Modeling of Direct-Drive Cryogenic Implosions,” submitted to *Physics of Plasmas*.